On the use of Kalman filters for high-order mode rejection in PZT-based microscanners

OPEN ACCESS
IOP Publishing
Journal of Micromechanics and Microengineering
J. Micromech. Microeng. **33** (2023) 044002 (9pp)
https://doi.org/10.1088/1361-6439/acbda8

On the use of Kalman filters for high-order mode rejection in PZT-based microscanners

Paolo Frigerio[1,*], Sara Cozzi[1], Luca Molinari[2], Andrea Barbieri[2], Roberto Carminati[2], Massimiliano Merli[2] and Giacomo Langfelder[1]

[1] Dipartimento di Elettronica, Informazione e Bioingegneria, Politecnico di Milano, Milan, Italy
[2] STMicroelectronics, Cornaredo, Italy

E-mail: paolo.frigerio@polimi.it

Received 20 November 2022, revised 7 February 2023
Accepted for publication 21 February 2023
Published 6 March 2023

Abstract
This work discusses and compares two strategies for closed-loop control of quasi-static silicon mirrors for raster-scanning applications, actuated by thin films of lead–zirconate–titanate and with embedded piezoresistive angular displacement sensors. A first feedback control approach, based on piezoresistive readout of the device angular displacement through an integrated sensor, shows limitations related to high-order resonant modes of the mechanical structure. To overcome this issue, a feedback control scheme based on the use of a Kalman filter to estimate the angular displacement and velocity of the scanner is presented, achieving a maximum positioning error of 0.14° (1.75% of a 8° full-scale angular displacement), and a mean error within ±0.03° (0.74% peak-to-peak) over 80% of the scanned trace.

Keywords: microscanners, piezoelectric actuators, PZT, Kalman filters

(Some figures may appear in colour only in the online journal)

1. Introduction

Silicon based microscanners are used to deflect laser sources in many different laser beam steering applications, ranging from miniaturized projectors [1] to virtual and augmented reality headsets [2], medical imaging [3] and LiDAR (light detection and ranging) [4]. They typically adopt either a raster-scanning architecture for image projection [5], or a Lissajous scheme for LiDAR applications [4]. In the latter, the two rotation axes of a bi-axial mirror are kept in simultaneous oscillation in order to produce a so called Lissajous projection pattern. In the former, two different actuation profiles are used for the horizontal axis and the vertical axis of the image. Either a single bi-axial mirror [6] or two separate uni-axial mirrors [7] are used. In both cases, the horizontal (or 'fast') axis is driven by a fast oscillator (with a frequency in the order of tens of kHz), thus generating a sinusoidal projection pattern, while the vertical (or 'slow') axis is driven by 60 Hz, 120 Hz, or up to 144 Hz triangular or sawtooth signals for high-resolution display applications [8]. A schematic example of the raster scanning architecture is represented in figure 1.

The vast majority of scanners presented in the literature are based on actuation via electrostatic forces [9] or electromagnetic coils [10]. However, a consolidating technology in recent years adopts the piezoelectric effect. Piezoelectric mirrors are actuated by films of piezoelectric materials, most prominently lead–zirconate–titanate (PZT), deposited on silicon cantilevers [11], which exploit the d_{31} piezoelectric coefficient [12] to strain the material in such a way to produce a bending of the cantilever, and thus a rotation of the mirror.

* Author to whom any correspondence should be addressed.

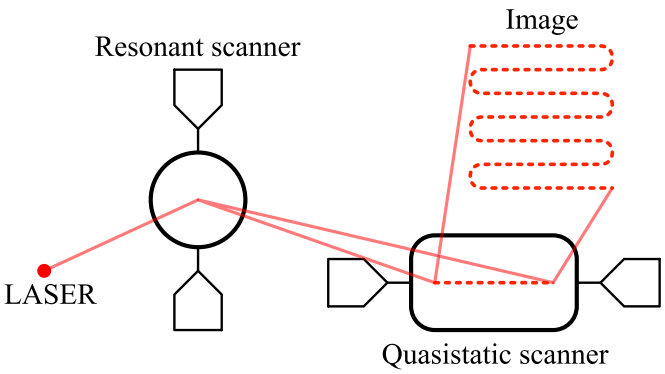

Figure 1. Schematic representation of a raster-scanning system based on two separate mirrors. The laser source is first directed onto the resonant scanner, which generates the horizontal scan line. This is in turn projected on the quasi-static scanner that steers it in the vertical direction, thus constructing the image according to the pattern sketched in the figure.

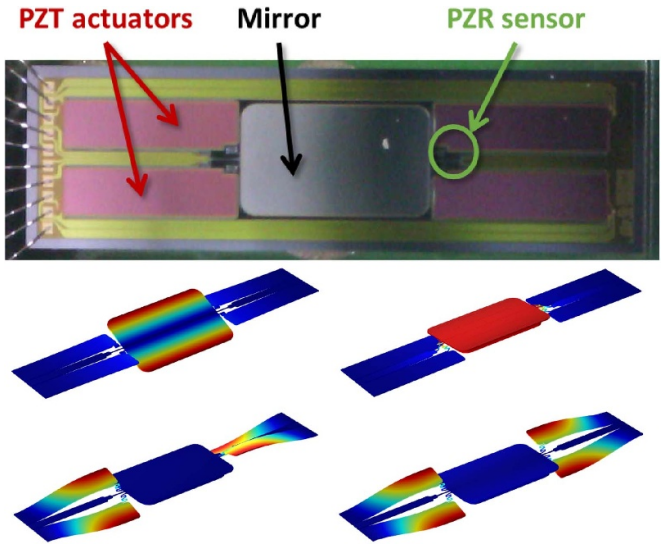

Figure 2. Picture of the mirror, showing the reflective coating, the position of the piezoresistive sensor, and the PZT actuators. Below the picture, the significant mode shapes of the device are shown.

The subject of this work is the accuracy of the control systems for the vertical scan, and it is thus focused on the quasi-static scanner of figure 1. This type of scanner is characterized by a low resonance frequency of the torsional eigenmode, ranging from few hundreds of Hz up to a few kHz, but a fairly large quality factor for the intended application, in the order of 50 to 100. These are both critical aspects for both open-loop and closed-loop control systems, and in turn for the final quality of the scan, as discussed in the following.

Figure 2 shows a microscope picture of a piezoelectric micromirror. The device is made by a large suspended silicon frame (2.4×1.44 mm^2), covered by a thin film of aluminum acting as the reflective surface. Such mass is suspended by silicon torsional springs defining the rotation axis. Four piezoelectric actuators surround the structure, and are realized by deposition of a 2- μm-thick PZT layer on top of silicon cantilevers, sandwiched between metal electrodes. These piezoelectric capacitors are short-circuited in pairs by metal traces deposited on the device die, so to achieve differential actuation. To produce a rotation of the structure, the two pairs are stimulated by anti-phase sawtooth signals.

Figure 2 also reports the relevant mode shapes of the device. The torsional mode (left) has a resonance frequency of 1.05 kHz. Additional mode shapes include in-plane and out-of-plane translations (center) and resonances of the piezoelectric cantilevers (right). Their eigenfrequencies are found at 5.84 kHz and 9.57 kHz, and pose a significant challenge to the electronic control scheme, as discussed in the following.

The instantaneous angular displacement is sensed via a piezoresistive sensor directly embedded on the device, and realized by n-type diffusion of four piezoresistors at the anchor point of one of the suspending springs. These elements are sensitive to the stress generated by the device, and, arranged in a suitably biased Wheatstone bridge configuration, they produce a differential voltage which is linearly proportional to the angular displacement [13]. The resistors are arranged as shown in figure 2 and are contacted by metal traces that run on the suspended cantilever where the torsional springs are attached. As known from the literature, the sensitivity of such type of sensor typically suffers from a significant temperature dependence [13], showing a linear trend with a negative first order coefficient. Such dependence can be compensated in the digital processing stages by adjusting a temperature-dependent gain according to information provided by a dedicated temperature sensor. Furthermore, PZR is also known to suffer from long-term drift, especially when humidity of the surrounding environment is uncontrolled [14]. To cope with moisture, either a buried structure can be used, as shown in [15], either a passivation layer is deposited on top of the structure to act as a barrier [16], as it is the case for the device under discussion.

Important figures of merit in defining the projected image resolution are the refresh rate, determined by the speed of the vertical scan, and the number of pixels that can be projected within each axis. This number depends not only on the maximum tilt angle that can be achieved by the micromirror, but also on its diameter, which limits the pixel size by diffraction, as well as on the accuracy of the electronic drivers. In order to avoid distortion of the image, the drivers and the control systems should achieve a high level of linearity and repeatability of the scan traces. Since each vertically scanned trace is essentially a ramp, its accuracy is quoted in terms of deviation of the measured trace from a straight line, i.e. with respect to a first-order polynomial fitting. It is also quoted in terms of repeatability, which describes the amount of noise that affects the displacement of each pixel in consecutive traces.

Accurate position control of MEMS micromirrors has been thus the topic of previous works. Since quasi-static scanners are typically driven by sawtooth signals, the main requirements of the position control system are: (a) to produce an artificial damping of the quality factor, so to avoid stimulating underdamped mechanical vibration at the resonance frequency, and (b) to artificially increase the bandwidth up to a few kHz, so to obtain accurate tracking of the reference signal and linearity errors within few tens of milli-degrees.

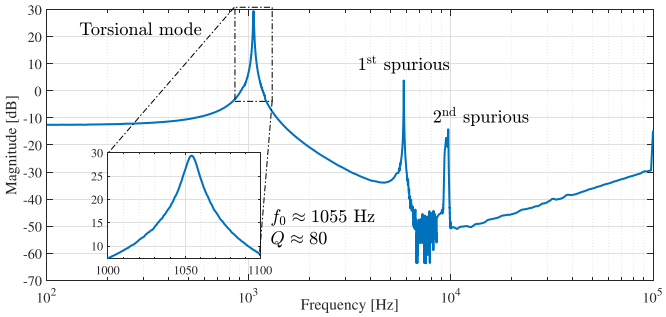

Figure 3. Measured transfer function of the mirror, showing spurious modes. The resonance frequency and quality factor of the torsional mode are reported in the figure, and evaluate to 1055 Hz and 80, respectively. Spurious modes are located at approximately 5.84 kHz and 9.57 kHz.

To achieve this, different approaches have been discussed, either using open- or closed-loop solutions.

Among the most basic open-loop approaches are the ones based on a shaping of the actuation signal: in [17] the authors propose 'flattening' the sharp triangle edges by saturation, while in [18] an approach based on limitation of the jerk applied to the mirror is discussed, resulting in a custom profile for the actuation signal. The positioning errors obtained in these works are in the order of 0.57°.

In more advanced solutions a suitable pre-filter is applied to the reference signal to suppress frequency components around the resonance frequency of the device, either by implementing a static [19] or dynamically-varying [20] filter. The errors achieved in these works are in the order of 0.2° for a trace with a 80% linear interval.

A review of closed-loop approaches is discussed in [21], based on variants of PID (proportional-integral-derivative) controllers. All these works are focused on scanners with either electrostatic or electromagnetic actuation, and thus fail to discuss a peculiar aspect of piezoelectric based devices.

Indeed, the combined use of piezoelectric actuators and piezoresistive sensing introduces a new challenge, which is illustrated in figure 3. Given the large size of the actuators, the natural resonance frequency of the cantilevers and actuators is too close to the torsional resonance, as visible from the resonant modes shown in 3. The displacement of the actuators exerts a stress on the piezoresistive sensor, thus a peak appears in the sensor output spectrum, however it does not translate into a significant tilt of the mirror mass due to its large inertia. Thus, the electrical signal provided by the PZR sensor contains both information on the actual tilt of the mirror, as well as the displacement of the actuators. If not properly managed, this spurious coupling undermines the implementation of a wide-bandwidth control system. This is mandatory to obtain linearity errors in the order of a few tens of degrees. Indeed, the controller required for obtaining a large bandwidth requires at least one zero in the transfer function to properly stabilize the rotational mode: such zero boosts the high-frequency transfer function, amplifying the spurious effect associated to the peaks around 5.84 kHz and 9.57 kHz.

In this work we compare, through both simulations and experimental validation, a standard closed-loop feedback approach with a modified strategy based on the use of a Kalman filter (KF) to improve command tracking of the piezoelectric microscanner of figure 2.

In the literature, state-observers have been adopted for position control of MEMS micromirrors. For example, in [22] an extended Luenberger observer has been applied to an electrostatic microscanner to improve the robustness of closed-loop control against model inaccuracies. In [23] an unscented Kalman filter (UKF) was used to estimate the states of an electromagnetic micromirror in presence of non-linear hysteresis, however discussing only simulation results. In [24] a UKF was used to estimate the states of two scanning mirrors, one electrostatic and one electromagnetic, for LiDAR applications, providing experimental results by measuring the angle via laser Doppler vibrometry, obtaining an accuracy in the estimation of the tilt angle within about 0.05°.

In this work we start from a standard PID control strategy, and extend it using a Kalman filter which is initially modeled on the linearized torsional dynamics of the mirror. We then extend the Kalman filter to include non-linear effects in the stiffness of the suspending springs, which cause both an increase of the resonance frequency and a variation of the actuation efficiency as a function of the instantaneous tilt angle. The aim is to improve robustness against the coupling of spurious modes to the position sensor by estimation of the desired torsional states. Thus the paper is organized as follows. In section 2 the physical modeling of the device is presented. In section 3 two alternative strategies for controlling the angular displacement of the reflective surface are presented, along with their circuit implementation. In section 4 experimental data comparing the performance of both strategies are presented, and in section 5 the critical aspects of both implementations are discussed with the aid of simulation data.

2. Device modeling

The device is modeled according to figure 4. Each *i*th eigenmode of the structure is described by a single degree of freedom system, represented by the equation of motion:

$$J_i\ddot{\theta}_i + b_i\dot{\theta}_i + k_i(\theta_i)\theta_i = \eta_i V_{\mathrm{PZT}} \tag{1}$$

where, depending on the type of displacement, J_i is the mass or mass moment of inertia, b_i is the linear or torsional damping coefficient, $k_i(\theta_i)$ is the displacement-dependent linear or torsional stiffness, η_i is the PZT transduction coefficient, transforming the applied voltage V_{PZT} into an equivalent force or torque, and θ_i is the linear or angular displacement of the *i*th mode. The voltage V_{PZT} is the difference between the two anti-phase voltages V_{DRVP} and V_{DRVN} applied to the two sets of actuators. The embedded piezoresistive sensor produces an output voltage proportional to the applied stress, which results as a superposition of the stresses exerted separately by each eigenmode, with the stress itself proportional to the linear and angular displacements. Thus, the sensor output voltage

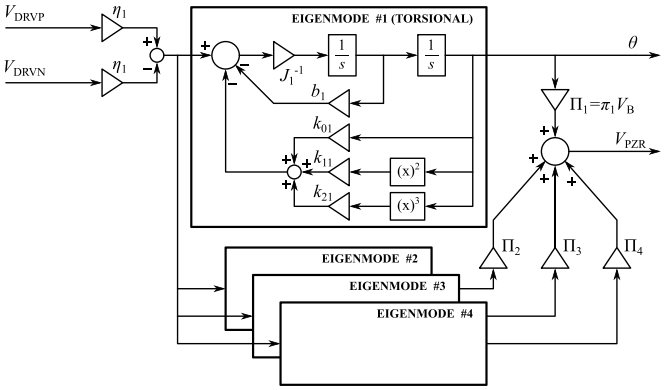

Figure 4. Block scheme of the microscanner model. Each eigenmode is represented by a replica of the model illustrated for the torsional one. The output of each mode is summed, with appropriate weight, to produce the output of the piezoresistive sensor.

Table 1. Parameters of the torsional eigenmode.

Parameter	Symbol	Value
Resonance frequency	ω_1	≈1 kHz
Quality factor	Q_1	≈80
Sensor nominal resistance	R_B	3 kω
Sensor bias voltage	V_B	3 V
Sensor transduction	Π_1	2.4 mV/deg
Actuator transduction	$\eta_1 J_1^{-1} \omega_1^{-2}$	0.2 deg/V

V_{PZR} is obtained by the weighted sum of the angular displacement associated to each eigenmode with appropriate coefficients $\Pi_i = \pi_i V_B$, where π_i is the resistance variation per unit angle, and V_B is the 3-V bias voltage of the sensor.

Neglecting the non-linear behavior of the stiffness, the relation between applied and readout voltage can be described by the sum of N second order transfer functions, with N representing the number of eigenmodes included in the model. The total transfer function is thus:

$$H_m(s) = \frac{V_{PZR}}{V_{PZT}} = \sum_{i=1}^{N} \frac{K_i}{s^2 + 2\xi_i \omega_i s + \omega_i^2} \tag{2}$$

where $K_i = \Pi_i \eta_i J_i^{-1}$ is the total DC gain of the transfer function of the ith mode, $\omega_i^2 = k_{0i} J_i^{-1}$ is the natural frequency, defined via the linear stiffness k_{0i}, and $2\xi_i = Q_i^{-1}$ is the damping ratio, with Q_i being the quality factor associated to the ith eigenmode. A list of the relevant parameters of the scanner is provided in table 1. Note that the factor K_i can be very large for high-order modes, even if these do not significantly affect the angle, thus complicating compensation of the effective mirror torsion when only using the information from the sensor.

The parameters of the device are obtained by finite element analysis and confirmed by experimental data. The resonance frequency ω_i and quality factor Q_i for each mode are directly measured by the plot shown in figure 3, while the moment of inertia J_i is obtained by numerical simulation. The damping coefficient is then calculated as $b_i = \omega_i J_i / Q_i$.

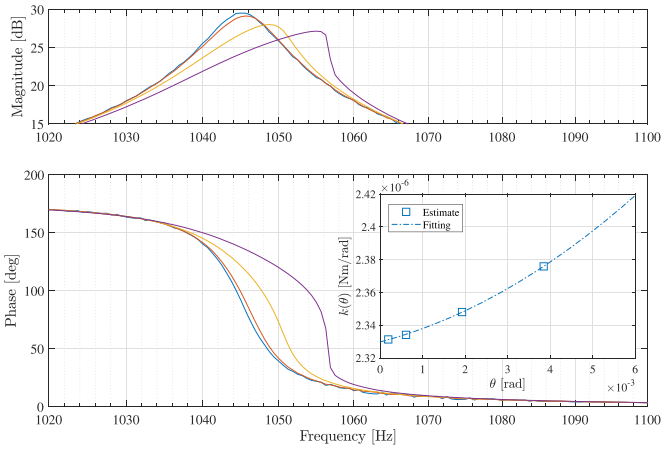

Figure 5. Estimation of the non-linear stiffness of the device from non-linear transfer function measurements.

Table 2. Coefficients describing the non-linear stiffness.

k_{01} (N m rad^{-1})	k_{11} (N m rad^{-2})	k_{21} (N m rad^{-3})
2.33×10^{-6}	6.82×10^{-6}	1.5×10^{-5}

For the Kalman filter implementation, the non-linear behavior of the stiffness must be characterized. To this aim, it is represented by a second-degree polynomial:

$$k_i(\theta_i) = k_{0i} + k_{1i}\theta_i + k_{2i}\theta_i^2 \tag{3}$$

where k_{0i} is the stiffness for small angular displacements, and the coefficients k_{1i} and k_{2i} are estimated by acquiring the transfer function of the device, using a network analyzer, for increasing actuation voltages and measuring the resonance frequency corresponding to the 90° phase-shift. Such frequency is approximately described by:

$$f_{0i} \approx \frac{1}{2\pi} \sqrt{\frac{k_{0i} + k_{1i}\theta_i + k_{2i}\theta_i^2}{J_i}}. \tag{4}$$

Inverting the previous equation, a curve as the one shown in the inset of figure 5 for the fundamental torsional eigenmode is obtained, where the angle is approximated as $\theta_i \approx V_{PZT} \eta_i Q_i k_{0i}^{-1}$. The non-linear coefficients are thus obtained by a polynomial fitting of such curve. The extracted values for the peak resonant mode are listed in table 2.

3. Control architectures

3.1. Standard feedback control

The standard feedback control technique is represented in figure 6. It is based on two loops for simultaneous control of both the angular velocity and displacement of the scanner. The electronic gain blocks G_d and G_{INA} represent the PZT driver and PZR sensor front-end, respectively. The high-order

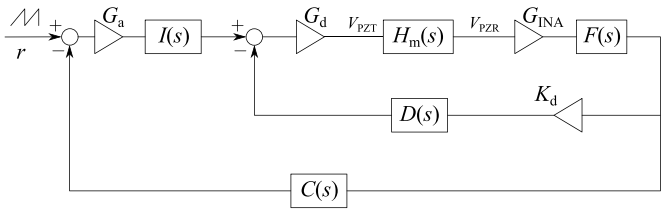

Figure 6. Standard feedback control block scheme. G_a represents the gain of the analog driver, while G_{INA} represents the gain of the sensor front-end (an INA). The dynamic part of the front-end is represented by the filter F. Speed and displacement control is performed by two separate control loops.

resonant modes are filtered by the block labeled $F(s)$, which contains a cascade of notch and low-pass filters tailored to the center frequency of the spurious resonant modes. The transfer function is:

$$F(s) = \frac{b_0 + b_1 s + b_2 s^2}{a_0 + a_1 s + a_2 s^2} \frac{c_0 + c_1 s + c_2 s^2}{d_0 + d_1 s + d_2 s^2} \left(\frac{\omega_p}{\omega_p + s} \right)^n \qquad (5)$$

where the filter coefficients a_j, b_j, c_j and d_j, with $j = 0, 1, 2$, ω_p and n are chosen to produce notch filters with center frequency matching the spurious resonance frequencies and a number n of simple low-pass filters. This ideally produces an output proportional to the displacement of the main mode only.

This output is processed by a loop made of a derivative block $D(s)$ which controls the device speed by suitably tailoring the gain labeled K_d. Its transfer function is:

$$D(s) = \frac{s}{(s + \omega_{p1})^2} \qquad (6)$$

where $\omega_{p1} \gg \omega_1$. This produces an artificial damping of the device quality factor and simplifies the design of the position controller. The closed-loop damping is set to 0.7 by simply adjusting the value of gain K_d. Since the quality factor of the torsional mode is larger than 10, the closed-loop quality factor can be set independently of the torsional Q with an error smaller than 10%, which is acceptable for the secondary loop. The sensor output is also processed by a second loop with a block $C(s)$ containing a phase-lead compensator for boosting the high-frequency response and thus increase the closed-loop bandwidth:

$$C(s) = \frac{s + \omega_{zc}}{s + \omega_{pc}} \qquad (7)$$

with $\omega_{zc} = \omega_1$ and $\omega_{pc} \gg \omega_1$.

The minimum required bandwidth for an adequate tracking of the reference sawtooth signal r was estimated as approximately 3 kHz in previous works [25, 26]. The error signal produced by such loop is processed by a real integrator $I(s)$ containing a zero in the transfer function for proper compensation and minimization of the error signal.

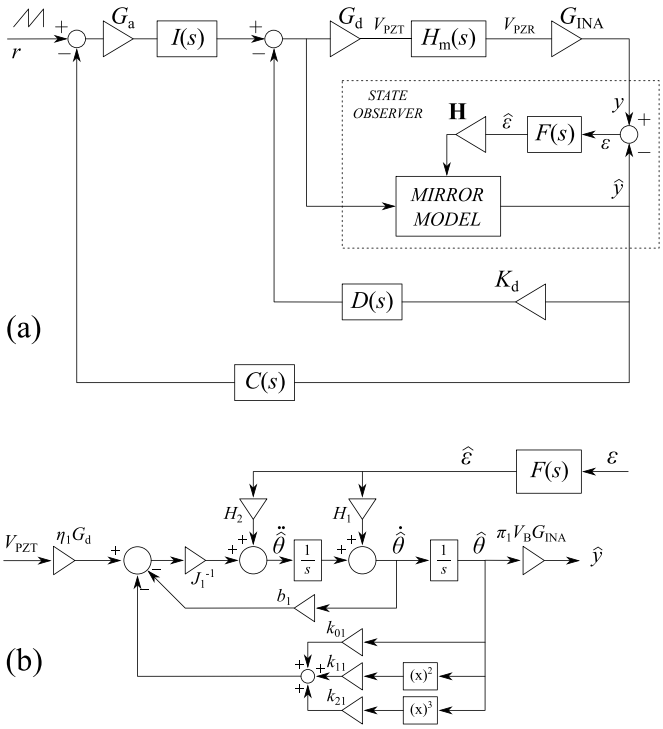

Figure 7. (a) Feedback control based on a state observer: the mirror states are predicted based on the model of figure 4, with additional terms to correct the convergence of the error. (b) Continuous-time model of the observer.

3.2. State observer design

The predictor-based control strategy is illustrated in figure 7(a), and it is an extension of the previously described approach. A state observer, modeled on the torsional mode of the mirror, as represented in figure 7(b), is used to predict the rotation dynamics. In principle the observer should be designed including all the observable states of the plant, i.e. the mirror; however, we chose to implement only the torsional mode to avoid requiring accurate calibration of each mode. The error ε between the PZR sensor output y and the estimated output $\hat{y}$ is filtered adopting a similar scheme $F(s)$ to the one used in the standard architecture, then multiplied by the error feedback vector $\mathbf{H} = (H_1\ H_2)^T$ in order to correct the estimated states with information measured from the sensor. Given the presence of spurious modes, the sensor output is filtered to only retain information in the low-frequency range where the mode of importance lies. Thus, the observer design is carried out modelling the main torsional mode described by (1), and adding the state correction via the measured estimation error ϵ. The integral operations are discretized in time to enable its implementation on a FPGA. This operation results in the following set of equations for estimation of the kth sample of angular displacement $\hat{\theta}$, angular velocity $\dot{\hat{\theta}}$ and the sensor output voltage $\hat{y}$:

$$\hat{\theta}_k = \hat{\theta}_{k-1} + \frac{T_s}{2}\dot{\hat{\theta}}_k + \frac{T_s}{2}\dot{\hat{\theta}}_{k-1} \qquad (8a)$$

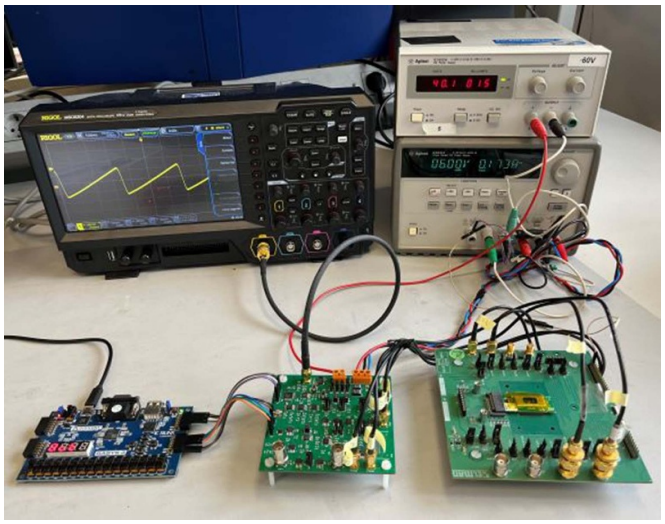

Figure 8. Picture of the experimental setup, with the three PCBs in front and the instrumentation on the back. From left to right: the FPGA hosting board, the interface board, and the mirror hosting board.

$$\begin{aligned}\dot{\hat{\theta}}_k = \dot{\hat{\theta}}_{k-1} &+ \frac{T_s\eta_1 G_\mathrm{d}}{2J_1}V_{\mathrm{PZT},k} - \frac{T_s k_{01}}{2J_1}\hat{\theta}_k - \frac{T_s k_{11}}{2J_1}\hat{\theta}_k^2 \\ &- \frac{T_s k_{21}}{2J_1}\hat{\theta}_k^3 + \frac{T_s H_2}{2}\hat{\varepsilon}_k + \frac{T_s\eta_1 G_\mathrm{d}}{2J_1}V_{\mathrm{PZT},k-1} \\ &- \frac{T_s k_{01}}{2J_1}\hat{\theta}_{k-1} - \frac{T_s k_{11}}{2J_1}\hat{\theta}_{k-1}^2 - \frac{T_s k_{21}}{2J_1}\hat{\theta}_{k-1}^3 \\ &+ \frac{T_s H_2}{2}\hat{\varepsilon}_{k-1} + H_1\hat{\varepsilon}_k \end{aligned} \tag{8b}$$

$$\hat{y}_k = G_\mathrm{INA}\Pi_1\hat{\theta}_k. \tag{8c}$$

The parameters H_1 and H_2 are used to define the observer dynamics, and are calculated using the linear–quadratic–Gaussian theory [27]. The weights R and $\mathbf{Q}$ of the Kalman filter are chosen according to the model: R is a scalar value modeled on the front-end noise, while $\mathbf{Q}$ is a 2×2 matrix chosen to improve the estimation error dynamics. In our tests we chose:

$$R = S_\mathrm{n}\cdot f_{\mathrm{BW,INA}} \approx (7\mu V)^2 \tag{9}$$

$$\mathbf{Q} = \begin{pmatrix} 0.1 & 0 \\ 0 & 0.1 \end{pmatrix} \tag{10}$$

where $S_\mathrm{n} \approx 2\cdot(7\mathrm{nV}/\sqrt{\mathrm{Hz}})^2$ is the measurement noise power spectral density introduced by the INA and the piezoresistors, and $f_{\mathrm{BW,INA}}$ is the bandwidth of the INA front-end, which defines the variance of measurement noise, and it is approximately 500 kHz. The estimated states are then used to close the control loop in a similar fashion to the standard architecture.

3.3. Circuit implementation

Both architectures have been implemented as a mixed-signal circuit, where both the predictor and controller fully belong to the digital domain. The front-end G_INA is implemented by an Instrumentation Amplifier (INA), followed by a 16-bit differential $\Sigma\Delta$ analog-to-digital converter ($\Sigma\Delta$-ADC). The PZT driver is implemented by a differential amplifier: its input is provided by a 16-bit digital-to-analog converter which translates the output word calculated by the controller from the digital to the analog domain. Figure 8 shows the experimental setup, comprised of three main boards: one hosts the FPGA (an Artix-7 by Xilinx) which is dedicated to the generation of the reference waveform (with no pre-filtering) and to the calculation the control law, a second board hosts the analog circuitry, and the third one hosts the mirror. The Kalman filter estimates and the control law are calculated with a frequency of 1 MHz. Results are assessed by acquiring the ADC output word, whose low-frequency components are proportional to the mirror angular displacement. The angle is computed with the following formula:

$$\theta = \left(\frac{D_{\mathrm{out,ADC}}}{2^n} - \frac{1}{2}\right)\frac{V_{\mathrm{REF,ADC}}}{G_\mathrm{INA}\pi_1 V_B} \tag{11}$$

where $D_{\mathrm{out,ADC}}$ is the decimal value of the ADC output word, $V_{\mathrm{REF,ADC}}$ is the ADC reference voltage (2.5 V), $n = 16$ and is the number of bits.

4. Results

Results are assessed in terms of linearity and reproducibility of the scanning trace. These are, respectively, defined as the deviation of each trace with respect to an ideal ramp, and the standard deviation of the position of each point on the trace between subsequent cycles. Linearity is obtained by isolating each trace and subtracting a first-order polynomial fit, subsequently averaging a number of traces to filter out white noise. Reproducibility, on the other hand, is evaluated without any averaging as it is a measure of noise.

Figure 9 shows the linearity measured on the same mirror sample with the two system architectures. The orange curve is obtained from the system adopting the standard feedback technique, while the blue one refers to the observer-based architecture. The former solution attains a non-linear error, measuring a value of $\pm 0.06°$ from 10% to 90% of the trace. Comparatively, the latter solution improves the flatness of the linearity error, which remains limited within $\pm 0.03°$ from 10% to 90% of the trace due to a slow response at the onset of the trace, thus achieving a factor 2 improvement with respect to the standard architecture over the specified range. The error becomes large at the left and right boundary due to the finite bandwidth of the system: the control loop is not able to track the sharp edges of the sawtooth waveform, resulting in a distorted waveforms around the peaks, and thus to a larger error. Thus, the useful portion for projection is taken from 10% to 90%.

Figure 10 shows the linearity errors for five different samples of the mirror, that were obtained with only a minor adjustment (within 2%) of the non-linear parameters k_{11} and k_{21}, showing the repeatability of the results. The root mean

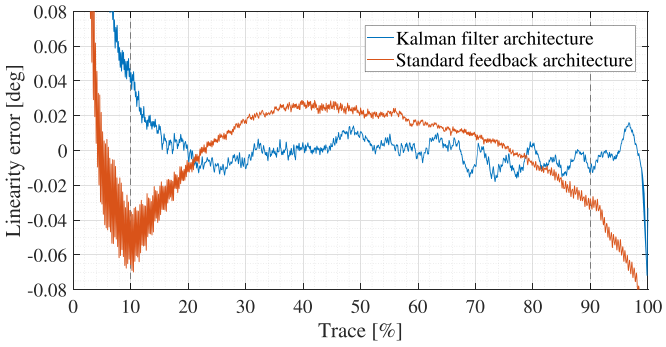

Figure 9. Comparison between the linearity obtained via the standard feedback and the Kalman-filter-based approach.

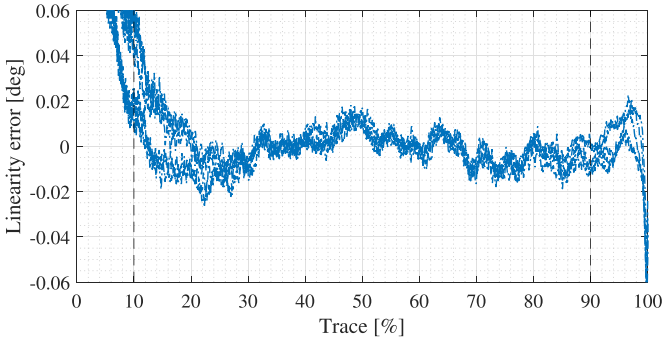

Figure 10. Linearity obtained with the Kalman filter for five different mirror samples. The traces show a good repeatability of the results.

Table 3. Standard deviation of linearity error and mean repeatability over five samples.

	Linearity (1σ) (mdeg)		Reproducibility (mdeg)	
DUT	standard	KF	standard	KF
1	29.94	9.89	12.67	16.19
2	27.52	8.70	13.48	15.66
3	37.15	10.55	13.31	15.64
4	33.43	8.21	13.02	15.42
5	36.98	8.83	12.36	15.85

square values of the errors of different devices under test (DUTs), evaluated over the 10%–90% range, are listed in table 3, along with the values of reproducibility. All the results are obtained acquiring the traces for 1 second, thus averaging the linearity measurement and evaluating the reproducibility over about 60 traces. The results listed in the table show that the Kalman filter enabled obtaining a three-fold reduction of the standard deviation of the error, while only increasing the trace reproducibility by about 25%. The table also shows that results are well repeatable across different samples of the same structure.

Table 4 lists the result obtained in this work compared to the literature survey provided in the introduction of the paper. It is worth noting, though, that an entirely fair comparison is not possible with all the works, as some employ lower actuation frequencies (i.e. 10 Hz) than our intended application.

Table 4. Comparison with other works, listing the error (peak-to-peak), the total field-of-view (FOV) and the actuation frequency.

Reference	This	[18]	[20]	[22]	[24]
Error (deg)	0.06	0.57	0.2	0.03	0.1
FOV (deg)	32	63	24	20	20
Freq. (Hz)	60	–	10	50	200

5. Discussion

The experimental results show a factor three improvement in the root mean square linearity of the traces obtained by control via state estimation. However, a proper trimming of the estimator parameters was needed, in particular of the constants that define the non-linear response. The impact of a mismatch between the mirror and the estimator parameters was performed via Simulink modeling of the system in order to assess the tolerance to such variations. As illustrated by the simulations in figure 11, the shape and maximum amplitude of the linearity error depends on parameter mismatch between the plant and the model. Both a mismatch in the actuation efficiency η_1 and the linear term of the spring stiffness k_{01} result in a gain mismatch between model and plant, and show the largest linearity errors, peaking up to $\pm 0.04°$. A mismatch of the quadratic term of the spring stiffness k_{11} instead shows a quadratic error, whereas a mismatch in the cubic term k_{21} shows a cubic error, as expected. These were verified in preliminary measurements, and were nulled by proper trimming of the Kalman filter parameters. Additionally, a mismatch of the linear term of the stiffness k_{01} also implies a mismatch of the natural frequency, which, not compensated, would manifest as a superposition of oscillations at the natural resonance of the device on the tilt angle. A part to part spread of the frequency in the order of 5% is expected due to process non-uniformity. However, the estimator feedback showed effectiveness in compensating such effect, as it was no more observed as the weights H_1 and H_2 were properly tuned. By contrast, the non-linear contributions can only be compensated by an adequate modeling of the related parameters.

The measured linearity error also manifests the slow dynamics of the implemented observer. The start of the trace shows a transient response with an estimated time constant of about 1 ms, which is close to the bandwidth of the state observer loop. Increasing the weights **H** to extend its bandwidth eventually resulted in small spurious oscillations superposed to the trace, which were attributed to instability of the observer due to a non-perfect compensation of the spurious resonant modes. Indeed, simulations of the system with a 5% mismatch between notch frequencies and peak frequencies showed that the system is prone to instability if the modeling of high order modes is not sufficiently accurate. This was also true in the case of an implementation

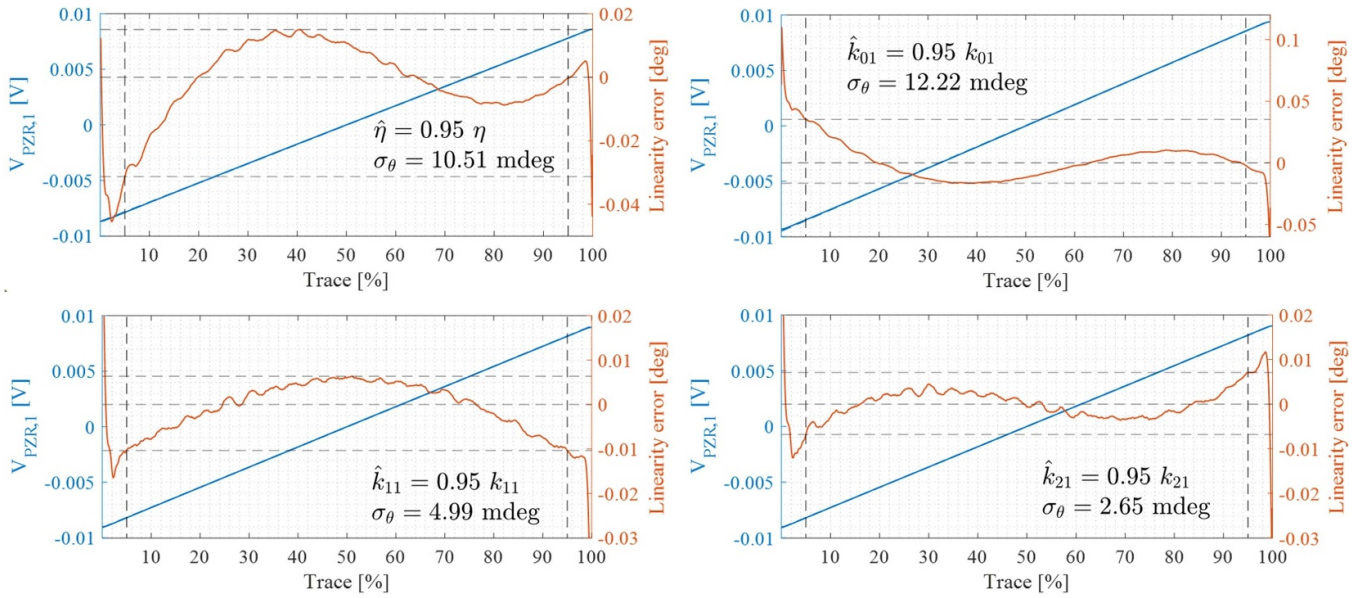

Figure 11. Simulations of mismatch. In each plot the average of traces acquired over 1-second simulations is shown against the corresponding line fitting error. Reported here are a mismatch of gain, described by the actuation efficiency η_1, a mismatch of natural frequency, described by the linear term of the stiffness k_{01}, and a mismatch of non-linearity within the stiffness, described both in terms of k_{11} and k_{21}. In all the cases a 5% mismatch between the parameter of the real mirror and its corresponding value within the model is considered.

based on a full Kalman filter with estimation of all the mode responses.

6. Conclusion

This work presented two strategies for position control of MEMS microscanners, discussing comparative results obtained from a more conventional feedback control system and from the same system augmented via state estimation. Results show that the use of a Kalman filter for estimating the mirror position and velocity improved by a factor three the root mean square of the scanned traces, while partially worsening the trace to trace repeatability. The best peak-to-peak linearity error is $\pm 0.03°$, with a mean repeatability of about $0.015°$ obtained across five different samples of the same mirror design. Given that the system is sensitive to the modeling of high-frequency modes, efforts of future work will be concentrated on finding an algorithm for automatic tuning of the parameters of the fundamental one, so to enable the implementation of a faster and more accurate estimator.

Data availability statement

The data that support the findings of this study are available upon reasonable request from the authors.

ORCID iDs

Paolo Frigerio https://orcid.org/0000-0002-3702-0625
Giacomo Langfelder https://orcid.org/0000-0002-2997-834X

References

[1] Conant R A, Hagelin P M, Krishnamoorthy U, Hart M, Solgaard O, Lau K Y and Muller R S 2000 *Sens. Actuators* A **83** 291–6
[2] Urey H, Wine D W and Lewis J R 1999 Scanner design and resolution trade-offs for miniature scanning displays *Proc. SPIE* **3636** 60–68
[3] Dickensheets D L and Kino G S 1996 *Opt. Lett.* **21** 764–6
[4] Wang D, Watkins C and Xie H 2020 *Micromachines* **11** 456
[5] Holmström S T S, Baran U and Urey H 2014 *J. Microelectromech. Syst.* **23** 259–75
[6] Wine D W, Helsel M P, Jenkins L, Urey H and Osborn T D 2000 Performance of a biaxial MEMS-based scanner for microdisplay applications *Proc. SPIE* **4178** 186–96
[7] Raboud D, Barras T, Conte F L, Fabre L, Kilcher L, Kechana F, Abelé N and Kayal M 2010 *Proc. Eng.* **5** 260–3
[8] Tauscher J, Davis W O, Brown D, Ellis M, Ma Y, Sherwood M E, Bowman D, Helsel M P, Lee S and Coy J W 2010 Evolution of MEMS scanning mirrors for laser projection in compact consumer electronics *Proc. SPIE* **7594** 75940A
[9] Jung D, Sandner T, Kallweit D and Schenk H 2012 Vertical comb drive microscanners for beam steering, linear scanning and laser projection applications *Proc. SPIE* **8252** 232–41
[10] Yalcinkaya A D, Urey H, Brown D, Montague T and Sprague R 2006 *J. Microelectromech. Syst.* **15** 786–94
[11] Urey H, Holmstrom S, Baran U, Aksit K, Hedili M and Eides O 2013 Mems scanners and emerging 3D and interactive augmented reality display applications *2013 Transducers & Eurosensors XXVII: The 17th Int. Conf. on Solid-State Sensors, Actuators and Microsystems (TRANSDUCERS & EUROSENSORS XXVII)* (IEEE) pp 2485–8
[12] Kempe V 2011 *Inertial Mems: Principles and Practice* (Cambridge: Cambridge University Press) (https://doi.org/10.1017/cbo9780511933899)

[13] Frigerio P, Di Diodoro B, Rho V, Carminati R, Boni N and Langfelder G 2021 *J. Microelectromech. Syst.* **30** 281–9
[14] Vergara A, Tsukamoto T, Fang W and Tanaka S 2021 *Sens. Actuators* A **332** 113131
[15] Nishimoto T, Shoji S and Esashi M 1994 *Sens. Actuators* A **43** 249–53
[16] Vergara A, Tsukamoto T, Fang W and Tanaka S 2022 *J. Micromech. Microeng.* **33** 014001
[17] Schitter G, Thurner P J and Hansma P K 2008 *Mechatronics* **18** 282–8
[18] Kyriakopoulos K J and Saridis G N 1988 Minimum jerk path generation *Proc. 1988 IEEE Int. Conf. Robotics and Automation* (IEEE) pp 364–9
[19] Janschek K, Schroedter R and Sandner T 2013 Flatness-based open loop command tracking for quasistatic microscanners *Dynamic Systems and Control Conf.* vol 56147 (American Society of Mechanical Engineers) p V003T37A001
[20] Schroedter R, Janschek K and Sandner T 2014 *IFAC Proc.* vol 47 pp 2685–90
[21] Milanović V, Kasturi A, Yang J and Hu F 2017 Closed-loop control of gimbal-less MEMS mirrors for increased bandwidth in LiDAR applications *Proc. SPIE* **10191** 157–69
[22] Schroedter R, Roth M, Janschek K and Sandner T 2018 *Mechatronics* **56** 318–31
[23] Zhao G, Dong R and Tan Y 2021 State estimation of MEMS electromagnetic micromirror systems by unscented Kalman filter *2021 CAA Symp. on Fault Detection, Supervision and Safety for Technical Processes (SAFEPROCESS)* pp 1–5
[24] Wang J, Zhang G and You Z 2019 *J. Micromech. Microeng.* **29** 035005
[25] Frigerio P, Molinari L, Barbieri A, Zamprogno M, Mendicino G, Boni N and Langfelder G 2022 *IEEE Trans. Ind. Electron.* **70** 1
[26] Frigerio P, Molinari L, Barbieri A, Carminati R, Boni N and Langfelder G 2021 Closed-loop control of quasi-static scanning pzt micromirrors with embedded piezoresistive sensing and spurious mode rejection *2021 21st Int. Conf. Solid-State Sensors, Actuators and Microsystems (Transducers)* (IEEE) pp 435–8
[27] Kalman R E 1960 *J. Basic Eng.* **82** 35–45